JOURNAL OF GEOPHYSICAL RESEARCH, VOL. 106, NO. D14, PAGES 15,233–15,249, JULY 27, 2001

Spatial and temporal variability of satellite-derived cloud and surface characteristics during FIRE-ACE

J.A. Maslanik,[1] J. Key,[2] C.W. Fowler,[1] T. Nguyen,[1] and X. Wang[2]

Abstract. Advanced very high resolution radiometer (AVHRR) products calculated for the western Arctic for April-July 1998 are used to investigate spatial, temporal, and regional patterns and variability in energy budget parameters associated with ocean-ice-atmosphere interactions over the Arctic Ocean during the Surface Heat Budget of the Arctic Ocean (SHEBA) project and the First ISCCP (Internatonal Satellite Cloud Climatology Project) Regional Experiment - Arctic Cloud Experiment (FIRE-ACE). The AVHRR-derived parameters include cloud fraction, clear-sky and all-sky skin temperature and broadband albedo, upwelling and downwelling shortwave and longwave radiation, cloud top pressure and temperature, and cloud optical depth. The remotely sensed products generally agree well with field observations at the SHEBA site, which in turn is shown to be representative of a surrounding region comparable in size to a climate-model grid cell. Time series of products for other locations in the western Arctic illustrate the magnitude of spatial variability during the study period and provide spatial and temporal detail useful for studying regional processes. The data illustrate the progression of reduction in cloud cover, albedo decrease, and the considerable heating of the open ocean associated with the anomalous decrease in sea ice cover in the eastern Beaufort Sea that began in late spring. Above-freezing temperatures are also recorded within the ice pack, suggesting warming of the open water areas within the ice cover.

1. Introduction

A primary emphasis of the First ISCCP Regional Experiment-Arctic Cloud Experiment (FIRE-ACE) and Surface Heat Budget of the Arctic Ocean (SHEBA) projects is the collection of suites of data sets able to support, through measurement of multiple parameters, detailed investigations of ice-ocean-atmosphere processes [*Moritz and Perovich, 1996*]. In particular, the April - July 1998 period addressed by FIRE-ACE encompasses the complex interactions among surface and atmospheric conditions that regulate the onset and rate of melt of the sea ice pack. Surface observations during this time provide a wealth of information on surface albedo, temperature, radiation, atmospheric conditions, and cloud cover at the SHEBA ice camp location during its drift in the Beaufort and Chukchi Seas in the western Arctic during October 1997-September 1998. In addition to these continuous point measurements, aircraft missions as part of FIRE-ACE and SHEBA mapped conditions within an approximately 60 x 60 km region centered on the location of the SHEBA camp during portions of the April - July 1998 FIRE-ACE study period.

The surface and aircraft observations are complemented by satellite imagery and sounder data acquired by a variety of platforms. These data provide the opportunity to determine the representativeness of the field measurements at the SHEBA site for other portions of the Arctic basin and for other time periods. Satellite-derived products can also serve as evaluation data sets and forcing fields for regional- and basin-scale modeling. Taken as a whole, the local-, regional-, and broad-scale observations provided by the network of surface observations, aircraft measurements, and satellite data collected during FIRE-ACE and SHEBA offer the opportunity for analyses across multiple scales at a level of detail not previously possible.

Such multiscale analysis is likely to be particularly relevant for the study of ice-ocean-atmosphere interactions during spring-summer 1998. The sea ice cover in the Beaufort and Chukchi Seas retreated to a record minimum, beginning with the unusually early formation of open water in May and June [*Maslanik et al., 1999a*]. Ice and oceanic conditions leading up to the melt season in 1998 were unusual [*McPhee et al., 1998*], with substantially thinner ice than is typical for the region and with considerable freshening of the ocean surface layer. Further, above-normal air temperatures and easterly to southerly winds during spring and summer favored enhanced melt and northward ice transport [*Maslanik et al., 1999a*].

A range of data sets are needed to investigate the mechanisms involved in such changes, and to test and improve the ability of models to simulate regional and local processes. The detailed observations provided by surface-based instruments and aircraft during SHEBA and FIRE-ACE are well suited to developing and testing process models. Other data sets acquired by satellite provide the means to extend the temporal and spatial sampling to larger areas. In particular, the availability of a consistent satellite-derived suite of products covering large areas over extended time periods, with relatively high spatial and temporal resolution, supports investigations of interactions among several parameters over a range of scales. Here we describe a comprehensive suite of products derived from advanced very high resolution radiometer (AVHRR) satellite imagery for the FIRE-ACE time period and apply these data to (1) investigate the temporal and regional variability in surface and atmospheric conditions in the western Arctic during April - July 1998, (2) determine how well conditions observed at the SHEBA site reflect conditions elsewhere in the region, and (3) consider the contribution of the

[1]Colorado Center for Astrodynamics Research, University of Colorado, Boulder.
[2]Cooperative Institute for Meteorological Satellite Studies University of Wisconsin, Madison.

Paper number 2000JD900284.
0148-0227/01/2000JD900284$09.00

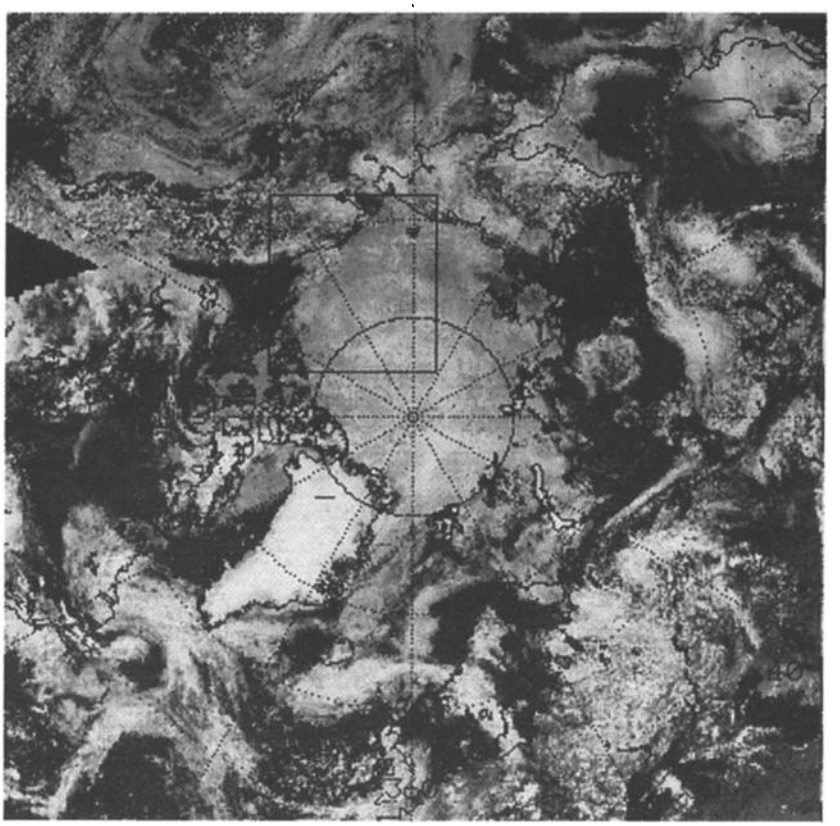

Figure 1. Example AVHRR-based Polar Pathfinder (APP) broadband albedo image for July 1998, illustrating the region of AVHRR Polar Pathfinder coverage for the Northern Hemisphere. The study area domain is indicated by the square.

observed conditions to the unusually large decrease in ice cover during summer 1998.

2. Data Sets

For this work, we make use of newly available AVHRR-based Polar Pathfinder (APP) products [*Meier et al., 1997*; *Maslanik et al., 1998*; *Schweiger et al., 1999; Maslanik et al., 1999b*] and additional products generated from the APP imagery. The AVHRR Polar Pathfinder, a part of the NOAA/NASA Pathfinder effort, is providing twice-daily composites at a 5-km resolution for June 1981 - 1998 using global area coverage (GAC) data and at 1.25-km resolution for 1995-1998 from local area coverage (LAC) and high-resolution picture transmission (HRPT) imagery (see http://polarbear.colorado.edu or http://nsidc.colorado.edu for more information). Products include twice-daily (approximately 0400 and 1400 LT) geolocated and calibrated radiances, clear-sky broadband albedo and skin temperature, solar zenith angle, satellite elevation angle, universal time coordinated (UTC) of acquisition, Sun-satellite relative azimuth angle (the absolute value of the difference between the Sun and the satellite azimuths), cloud mask, surface-type masks, and ice motion fields. The APP products are mapped to the Equal-Area Scalable Earth-Grid (EASE-Grid) [*Armstrong and Brodzik, 1995*], in common with other Polar Pathfinder data sets to facilitate combining products from different sensors [*Schweiger et al.*, 1999]. Areas of coverage for the APP products are poleward of 50°N and 53 °S. An example of the APP coverage for the Northern Hemisphere is shown in Figure 1.

For the April-July 1998 period, additional geophysical products were derived from the APP AVHRR data using Cloud and Surface Parameter Retrieval (CASPR) algorithms [*Key, 1999; Key et al., 1997a*; 1997b, *Key and Schweiger, 1998*; *Key and Intrieri, 2000*] for the region and locations indicated in

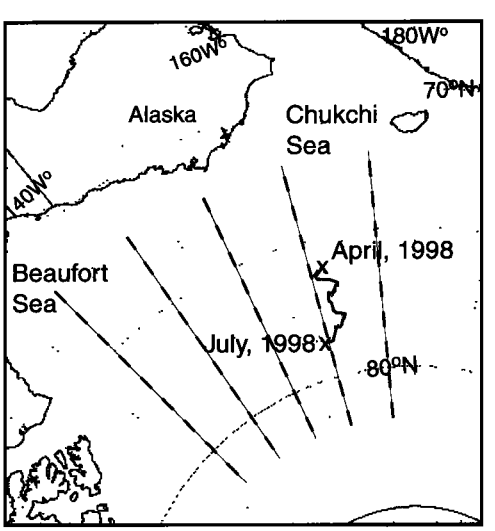

Figure 2. Details of the study area domain. Shown is the drift track of the SHEBA ice camp for April-July 1998 (starting and ending points shown by crosses), and the latitude and longitude transects selected for additional analyses.

Figure 2. These additional products include broadband albedo and surface temperature for all-sky conditions, downwelling and upwelling shortwave and longwave radiation, cloud top pressure, cloud top temperature, and cloud phase. The procedures for estimating surface and cloud parameters from the AVHRR and their relative accuracies are described in Appendix A.

To provide further information on sea ice conditions, we use passive-microwave derived ice concentrations from the Special Sensor Microwave/Imager (SSM/I) as obtained from the National Snow and Ice Data Center (NSIDC). The NSIDC-provided ice concentrations were re-mapped to the EASE grid and over-sampled to a 5-km grid spacing to facilitate comparisons to the AVHRR data. Observations from the SHEBA experiment used here include hourly measurements from the SHEBA Project Office (SPO) 10-m meteorological tower, and 10-min. observations from the NOAA cloud lidar and radar (provided by T. Uttal and M. Shupe of the NOAA Environmental Technology Laboratory). SPO and lidar/radar observations were selected from these data files to correspond most closely to 1400 LT. While these data sets continue to be refined and calibrated, they are well-suited to the comparisons performed here. Additional data sets, including sea ice charts prepared by the Navy-NOAA National Ice Center (NIC) and reanalysis fields from the National Centers for Environmental Prediction (NCEP), were used as background information, as described by *Maslanik et al.* [1999a].

3. Analysis Approach

To investigate spatial and temporal patterns and variability of surface and atmospheric conditions, the AVHRR-derived products for the FIRE-ACE period are analyzed as monthly means, composites, and time series. The 1400 LT composites of the APP AVHRR data for April 1 - July 31 1998 (a total of 122 days) for the 1875 x 2000 km region in Figure 2 were extracted from the full APP Northern Hemisphere grid, with the additional CASPR-derived products calculated for these subsets. Figure 2 also shows the drift track of the *Des Groseilliers* and the SHEBA field camp. Data were missing entirely for 18 days during this period due to a lack of available data from the sources used to supply the APP processing. The missing days of year were 106, 138, 140, 147-149, 151, 157, 160, 187-190, 194, 197-200, and 210. Some gaps in orbit coverages are present at random times and locations.

Initial examination of the all-sky products identified errors introduced by misidentified "clear-sky" pixels that contributed, via neighborhood interpolation, to errors in the estimated all-sky skin temperature and albedo. While future improvements in the cloud detection procedure will probably reduce these problems, for the purposes of this study the intermediate step was taken of filtering out these erroneous all-sky values. Temporal change detection was applied to identify pixels that exhibited a large decrease in skin temperature from one day to the next. These pixels were coded with a missing-data value and used subsequently to mask the corresponding pixels in the other all-sky CASPR products. Over the entire study domain, a mean of 10% of the pixels were filtered in this manner. Over ocean only (including open ocean and ocean area covered by ice), 7% of the pixels were filtered, indicating that the cloud detection problem was most prevalent over land for the data considered here.

For clear-sky albedo (α_{clr}) and skin temperature ($T_{s,clr}$), monthly composites were calculated using the original cloud mask. For each month, the last-occurring clear-sky data value was accumulated into clear-sky composites for that month, with one image generated per day. The images for each day of the month represent the composited data up until that date. The image for the last day of the month thus represents the composite of all clear-sky days in the month and are most characteristic of conditions within the last several days of the month. This approach was used, rather than calculating a monthly mean, since large changes in skin temperature and albedo are observed during each month. Means would thus tend to misrepresent conditions at specific times. Separate grids were created to store the date associated with the albedo and temperature value appearing in each composite. The composites for each day, as well as the grids containing the date used for the composite, provide a means of determining how well the composites represent conditions throughout the month.

For the all-sky products, monthly means were calculated at each pixel, with versions generated with and without the additional filtering noted earlier. Mean cloud fraction for each pixel was calculated as the count of cloudy days divided by the number of days with available data. Additional information such as the number of cases of two and three consecutive days of clear skies per pixel was also determined.

Time series of daily data were extracted for the 5-km pixel estimated to contain the reported position of the *Des Groseilliers* during the study period. Uncertainties in the pixel registration are estimated to be typically plus or minus 0.5 pixel. Thus the ship-based observations will fall within a 3 x 3 pixel (15 x 15 km^2) window in nearly all cases, but uncertainties will have some effect on the interpretations of the comparisons of surface-based and AVHRR-derived data. In addition, statistics were estimated for regions of various sizes centered on the single "ship" pixel. Windows of 11 x 11 pixels (55 x 55 km^2), 21 x 21 pixels (105 x 105 km^2), and 61 x 61 pixels (305 x 305 km^2) were used. Single-pixel transects were also extracted for various locations. Additional analyses made use of the coregistered SSM/I data to stratify the AVHRR products as a function of ice concentration.

4. Results

The time series of AVHRR-derived parameters provides a relatively detailed portrayal of the progression of cloud, surface, and radiation conditions during the April - July period. The results lend themselves to determining the degree to which measurements in the vicinity of the SHEBA site are representative of the larger, western Arctic area. Particularly apparent in these data is the range of variations that occur within the seasonal sea ice zone compared to the central ice pack. We begin by summarizing the parameters (Table 1) extracted for the SHEBA study region. These data are then considered in the

Table 1. Abbreviations and Symbols

Variable	Description
α_{clr}	broadband surface albedo (clear sky)
α_{all}	broadband surface albedo (all sky)
$T_{s,clr}$	skin temperature (clear sky)
$T_{s,all}$	skin temperature (all sky)
$S\downarrow$	downwelling shortwave radiation at surface
$S\uparrow$	upwelling shortwave radiation at surface
$L\downarrow$	downwelling longwave radiation at surface
$L\uparrow$	upwelling longwave radiation at surface
Ac	cloud fraction
Tc	cloud-top temperature
Pc	cloud-top pressure
S_{net}	net shortwave radiation at surface
F_{net}	net longwave radiation at surface

Table 2. Monthly Means for 1400 LT for the 105 x 105 km^2 Region Centered on the SHEBA Field Camp for April-July 1998

Variable	April	May	June	July
$S\downarrow$ (W m^{-2})	298	407	526	377
	(95)	(104)	(97)	(96)
$S\uparrow$ (W m^{-2})	235	321	328	184
	(86)	(92)	(79)	(57)
$L\downarrow$ (W m^{-2})	241	263	268	288
	(16)	(23)	(21)	(31)
$L\uparrow$ (W m^{-2})	257	280	298	298
	(11)	(19)	(23)	(29)
Pc (hPa)	767	770	673	668
	(140)	(103)	(180)	(170)
Tc (K)	255	258	265	264
	(5)	(7)	(6)	(11)
α_{all} (%)	84	82	60	48
	(4)	(3)	(9)	(8)
$T_{s,all}$ (K)	258	264	271	270
	(2.7)	(4.6)	(5.5)	(7.0)
Ac	0.80	0.93	0.88	0.78
	(0.3)	(0.2)	(0.3)	(0.3)

Average monthly standard deviations are given in parentheses.

context of the overall conditions in the western Arctic Ocean through discussion of monthly means of selected parameters.

4.1. Conditions in the SHEBA Area

Tables 2 and 3 summarize monthly mean values of the AVHRR-derived parameters for the 105 x 105 km^2 region centered on the SHEBA field camp location. The monthly means capture the basic variations in the cloud and energy balance parameters measured at the SHEBA camp (Table 4). Monthly mean temperatures agree quite well in April and May, but with an underestimate in June and July, likely due to residual errors in the cloud detection. The greatest discrepancy occurs in downwelling shortwave radiation ($S\downarrow$.). The large difference is probably due to a difference in cloud amounts, where the AVHRR is reporting significantly more cloud than the surface observer for a number of days, the net effect of which is to decrease $S\downarrow$ and increase the downwelling longwave fluxes ($L\downarrow$). This is not necessarily incorrect, because the spatial variability in cloud cover is large. Additionally, some AVHRR data are missing in the latter part of April, which results in a negative bias in the monthly mean, and while the target time for the AVHRR data is 1400 local solar time (LST), the actual acquisition time can differ by up to 2 hours. The downwelling, upwelling, and net radiation budgets show a typical progression of spring-summer values, with a slightly negative net longwave budget and a maximum total net radiation budget in July.

The monthly mean cloud fractions (Ac) for the pixel containing the SHEBA camp location show some substantial differences compared to the fraction estimated from the SHEBA NOAA lidar/radar (Figure 3a), which probably account for a portion of the discrepancies between observed and AVHRR-derived downwelling and net radiative fluxes. The underestimate

Table 3. Net AVHRR-Derived Radiative Fluxes in W m^{-2} at the Surface Calculated From the Data in Table 2 for the 105 x 105 km^2 SHEBA Region

Variable	April	May	June	July
S_{net} (W m^{-2})	63	86	198	194
L_{net} (W m^{-2})	-16	-17	-30	-10
Total Net	47	69	168	184

Positive values denote energy input to the surface.

Table 4. Field Observations From the SHEBA Site

Variable	April	May	June	July
$S\downarrow$ (W m^{-2})	365	495	493	347
$S\uparrow$ (W m^{-2})	294	391	342	184
$L\downarrow$ (W m^{-2})	219	245	281	300
$L\uparrow$ (W m^{-2})	246	278	311	315
α (%)	81	79	69	53
T_s (K)	256	265	272	273
Ac(obs)	0.67	0.76	0.75	0.80
Ac(lidar/radar)	0.87	0.97	0.90	0.94

Ac(obs) are cloud fractions obtained by 6-hourly visual observations at the ship. Ac(lidar/radar) is from a combination of measurements from the NOAA lidar and radar systems. All others are from the SHEBA Project Office (SPO) 10-m meteorological tower. Albedo (α) is calculated as the ratio of $S\downarrow$/ $S\uparrow$. Ts is the SPO-provided estimate obtained from the tower's Eppley pyrgeometer.

relative to the lidar and radar data is not unexpected, given that the surface-based remote sensing instruments are sensitive to even very optically-thin cloud, including diamond dust (T. Uttal, personal communication, 1999). Also shown is the mean cloud fraction estimated using the temporally filtered cloud masking used to remove erroneous data from the all-sky CASPR products. Overall, the filtering has little effect on the means. Note also that large differences exist between the mean monthly cloud fraction reported by field observers and estimated using the lidar/radar system (Table 4). The AVHRR-derived cloud fractions for the 5-km pixel at the ship location (Figure 3a) agree most closely with

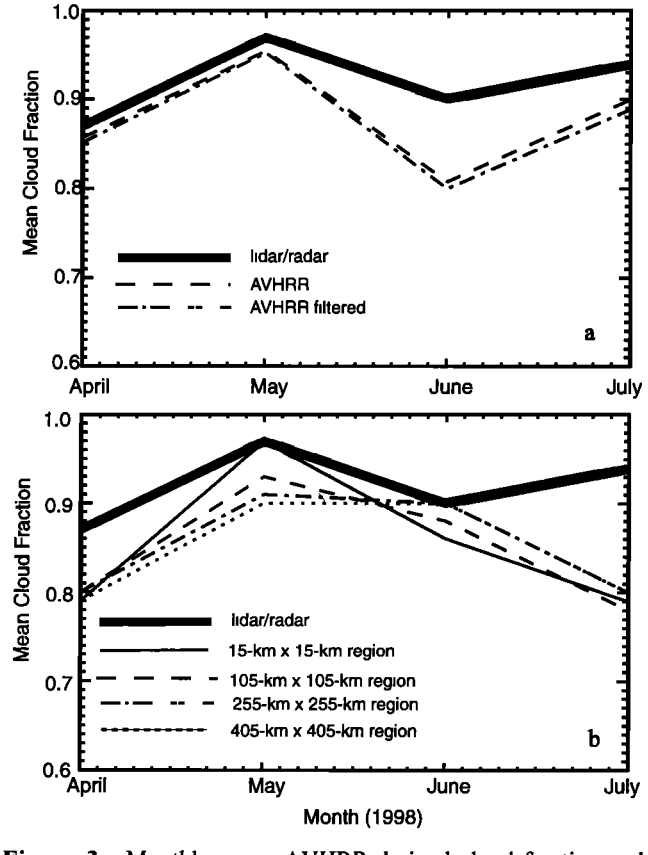

Figure 3. Monthly mean AVHRR-derived cloud fraction and cloud fraction observed by the NOAA LIDAR/RADAR at the SHEBA site. (a) Means for the site location (individual 5-km pixel for AVHRR). (b) Comparison of means averaged over different sizes of regions.

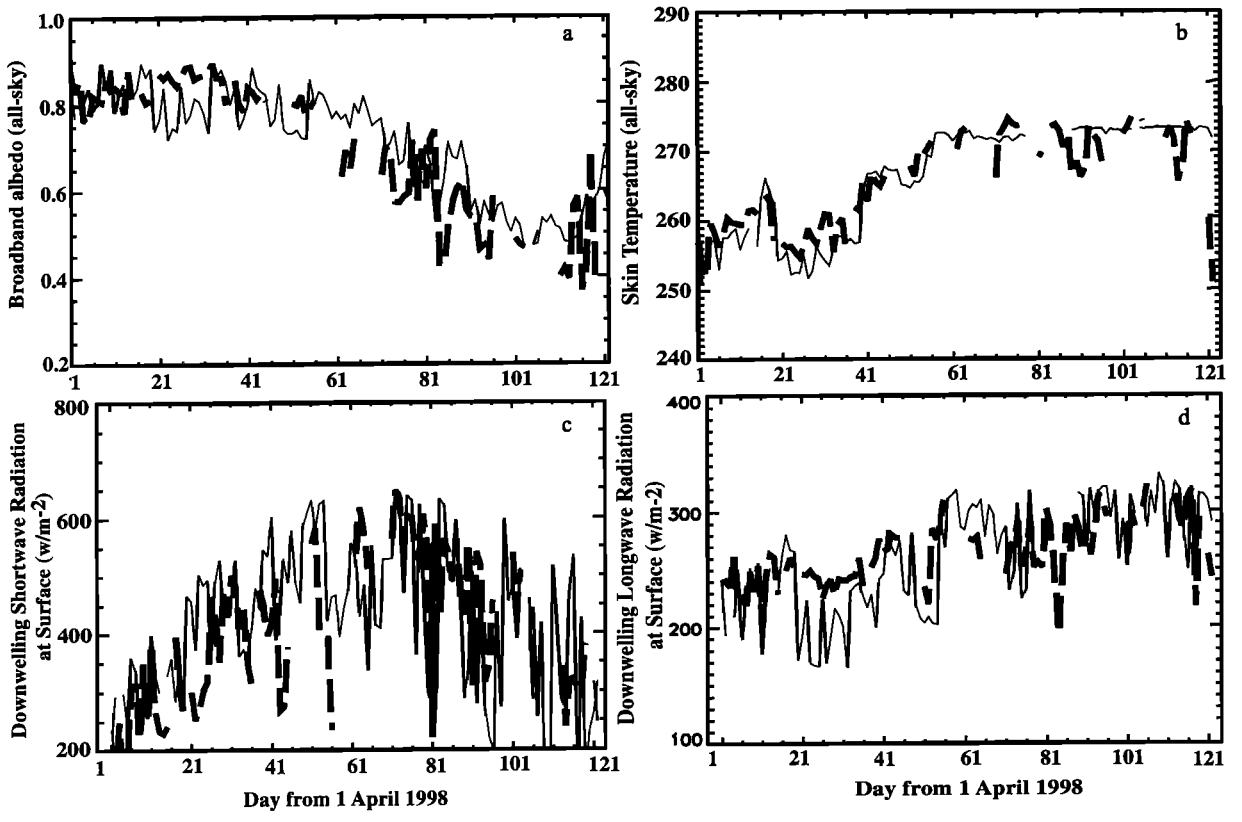

Figure 4. Comparison of daily (nominal 1400 LT) AVHRR-derived time series and field-measured data for (a) surface all-sky broadband albedo, (b) all-sky skin temperature, (c) downwelling shortwave radiation at the surface, and (d) downwelling longwave radiation at the surface. The thick dashed line represents AVHRR data. The solid line represents surface measurements.

the combined lidar/radar cloud retrievals, which might be expected given the remote sensing nature of the two data sets.

Mean cloud fraction for larger regions surrounding the ship location show some differences relative to the cloud fraction nearer the ship (Figure 3b). For regions ranging from 15 x 15 km^2 to 405 x 405 km^2 the fractions change relatively little, although averaging over an increasingly large area tends to reduce the month-to-month variability. However, averaging over the larger areas yields substantially less mean cloud in April and July compared to the single-pixel means at the ship location. Mean cloud fraction for individual pixels within the 3 x 3 pixel window centered on the ship location show greater cloud amount south of the center pixel (ship location) in April and west of the center pixel in July. This local variability might partially explain the underestimate of $S\downarrow$ during April.

Monthly mean cloud-top temperature and pressure (*Tc* and *Pc*) are also given in Table 2. The mean cloud-top pressures in April and May are similar but decrease (altitude increases) by nearly 100 hPa from May to June. The mean cloud-top temperature increases by 7 K from May to June in response to the warming troposphere. The weakening of the stable wintertime boundary layer and increased role of convection during the summertime at least partially explain the increase in cloud-top height.

When examined as daily time series, the AVHRR daily means for the 105 x 105 km^2 area are shown to capture much of the day-to-day variability present in the SPO field observations (Figures 4a-4d). In fact, the daily comparisons suggest better overall agreement for $S\downarrow$ and $S\uparrow$ than is indicated by comparing the AVHRR means in Table 2 to the surface observations in Table 4. Much of the underestimate in April occurs during a period in midmonth, while missing data during May contributes to some of the mean differences.

From these comparisons the SPO observations at the SHEBA camp appear to be representative of the larger "aggregate-scale" area comparable to a model grid cell. The apparent decrease in cloud cover away from the immediate (5 x 5 km^2) region of the ship does not have a particularly large influence on the other energy budget variables during the April - July period. However, if similar patterns hold for the cold months, then a greater effect could be expected due to net warming from the cloud cover.

4.2. Spatial and Temporal Scales

The spatial variability of surface and cloud properties was examined by averaging each parameter over boxes of 15, 25, 55, 155, and 305 km on a side, all centered on the SHEBA ship location. Normalized standard deviations as a function of spatial scale are given in Figure 5. The average standard deviations over the period April–July for each parameter were divided by the maximum standard deviation for the parameter so that all values were scaled into the range [0,1]. The maximum standard deviations used are given in the figure and can be used to invert the normalization.

The variance (or standard deviation) of all parameters increases with spatial scale. Overall, surface temperature variance increases with increasing spatial scale most rapidly and surface downwelling radiative flux variances increase at the lowest rate. However, cloud property variability increases most

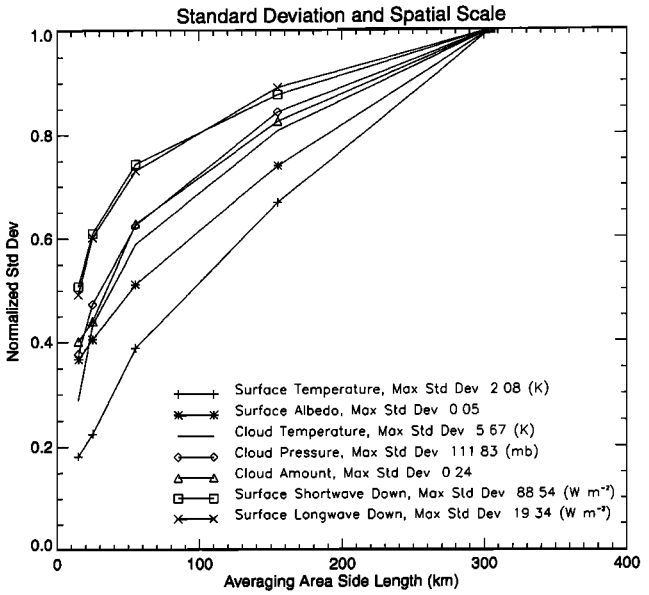

Figure 5. Normalized standard deviation of cloud and surface properties for different spatial scales. Average standard deviations over the period April–July for each parameter were divided by the maximum standard deviation for the parameter (given in the legend) for scaling into the range [0,1].

rapidly at the smaller spatial scales, i.e., from 5 to 25 km, and the radiative flux variability responds accordingly.

The temporal persistence of surface temperature, surface albedo, cloud temperature, and cloud amount was also examined. Figure 6 illustrates this as a semivariogram. The semivariance is the expected value of the squared difference between two observations of a random variable $Z(s)$ separated by some distance h:

$$\kappa(h) = \frac{1}{2} E\{[Z(s) - Z(s+h)]^2\} \quad (1)$$

where E is the expected value operator and h is the number of days. Similar to the normalized standard deviation in Figure 5, the semivariance of each parameter in Figure 6 is normalized by the maximum semivariance for that parameter. Mean values over the 105 x 105 km^2 spatial scale were used in the analysis. Results shows the greatest persistence at short timescales, indicated by low semivariance values. The time lag at which the semivariogram becomes asymptotic, called the "sill," describes the time lag beyond which the variance of the differences does not increase. For surface albedo the sill is reached after 60-70 days. Surface temperature semivariance has a similar pattern, though the variance at the shorter timescales is larger, and the sill is reached sooner, at a time lag of 50-60 days. Cloud temperature persistence is weak, and cloud amount shows almost no temporal correlation.

4.3. Regional Conditions

To facilitate analysis of the AVHRR products for the full study domain, monthly means were generated from the all-sky parameters, and composites were created for clear-sky surface albedo and skin temperature, as described earlier. Each of the products provides some insights into the uniformity of conditions in the western Arctic. They also depict the progression of conditions that contributed to the record retreat of the ice pack in 1998.

Figures 7 and 8 illustrate monthly mean AVHRR-derived all-sky broadband albedo and skin temperature extracted along longitude transects spaced at 10° intervals from 135°W to 175°W, as shown in Figure 2. The values plotted are areal averages for 105 x 105 km^2 areas centered at 2° latitude increments from 72°N to 82°N. Gradients along the transects reflect differences in the evolution of conditions within the seasonal ice zone compared to.the perennial ice pack and provide insight into how well the SHEBA area represents the larger region. Albedos are lower and skin temperatures tend to be higher in the eastern portion of the region. The effects of the removal of ice cover in the Beaufort Sea accentuates the month-to-month changes, including warming of the surface waters at the southern ends of the 135°W and 145°W transects.

Monthly mean cloud fraction for April-July (Figure 9) shows that the extensive cloudiness seen at the SHEBA site in May was prevalent over much of the Beaufort and Chukchi Seas. By June though, the distribution of cloud fraction was more meridional, with decreasing cloud cover in the eastern Beaufort Sea. This pattern continued into July, when the area of reduced cloud extended farther westward. This increase in cloudiness from April to May is seen in climatologies for the Arctic Ocean [e.g., *Schweiger and Key, 1992*] and appears typical of the western Arctic. *Serreze et al.* [1997] note that several cloud climatologies [*Warren et al., 1986; 1988*] and regional analyses of cloud cover [*Serreze and Rehder, 1990*] show that cloud cover tends to be reduced in the southern Beaufort Sea, particularly in summer, which is consistent with the patterns seen here for 1998. The spatial distribution of AVHRR-derived cloud fraction is also consistent with sea level pressure (SLP) patterns (Figure 10). High pressure dominated in the eastern portion of the study area, where cloud cover was reduced. Low pressure developed in the northern portion of the study area in July, where cloud cover is seen to be greater in Figure 9d. SLP was above normal in the eastern Beaufort Sea and Canadian archipelago during spring and

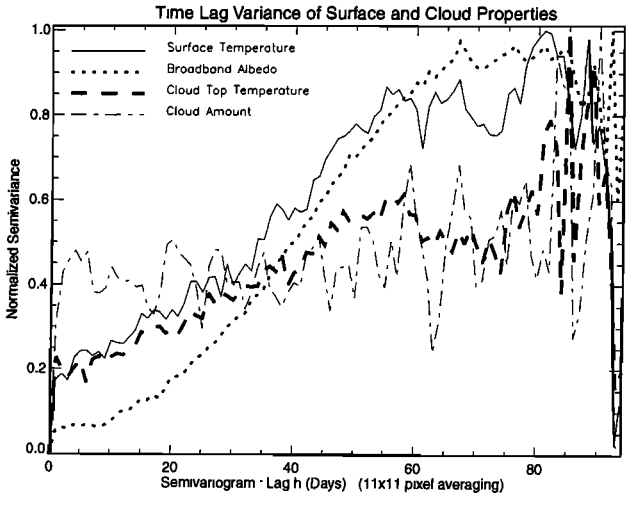

Figure 6. Time lag semivariogram for surface temperature, surface albedo, cloud temperature, and cloud amount. The semivariance is the variance of the difference between parameter values when separated by some number of days, given on the horizontal axis. The semivariance of each parameter is normalized by the maximum semivariance. Mean values over the 105 x 105 km^2 spatial scale were used in the analysis.

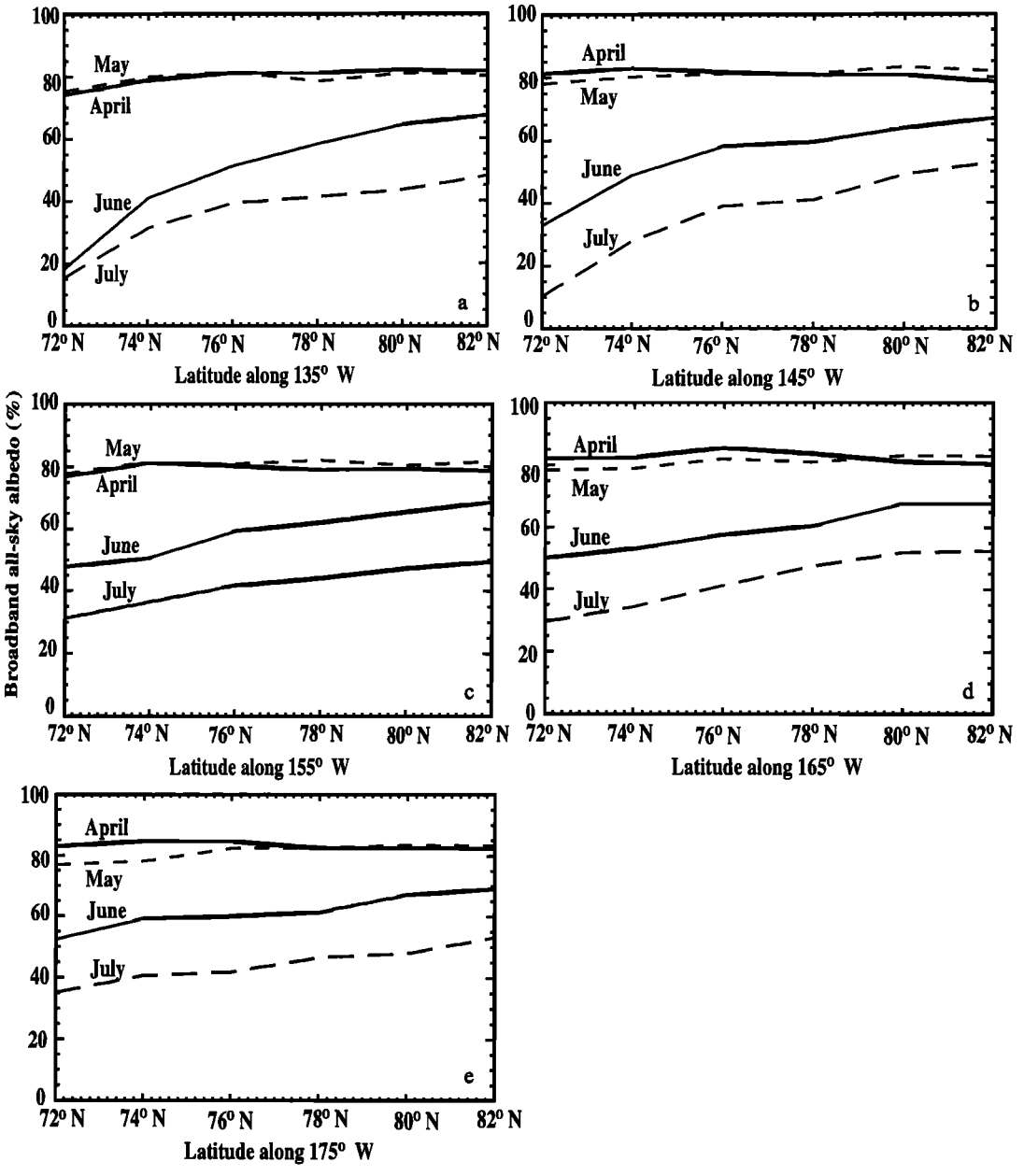

Figure 7. Monthly mean AVHRR-derived broadband all-sky albedo for 105 x 105 km^2 areas centered on 2° latitude increments from 72°N to 82°N, along (a) 135°W longitude, (b) 145°W, (c) 155°W, (d) 165°W, and (e) 175°W.

summer, a pattern typical of other years with below-normal sea ice extent at the end of summer [*Rogers., 1978; Maslanik et al., 1999a*]. This yielded stronger and more persistent easterly winds, which could have contributed to reducing the cloud cover initially in the eastern Beaufort Sea, since the air mass entering the eastern Beaufort originated over the relatively warm and dry land area. This may have also led to more clouds forming over the central and western Beaufort Sea as the air mass gained moisture from the open water and then traveled over the ice pack to the west. *Serreze and Rehder* [1990] suggest that such regional links between cloud cover and winds in the Beaufort Sea and Canada Basin area appear more related to local processes than to synoptic-scale pressure patterns. Local conditions were in fact unusual during the period, with open water areas forming earlier and over a greater area than seen previously, beginning in the eastern Beaufort and progressing westward [*Maslanik et al., 1999a*]. This increased amount of open water may have affected cloud cover, perhaps by providing a greater expanse of relatively warm surface area that was not conducive to formation of low-level stratus or by providing an additional moisture source to yield the increases in cloud cover seen farther to the west, under the influence of the easterly and southeasterly winds common during spring and summer.

This extension of open water area in May through July is apparent in the AVHRR products. Figures 11 and 12 show clear-sky composites for April and July, generated using the AVHRR-derived clear-sky broadband albedo and the cloud mask, with albedo composited through the entire month. A 3 x 3 median filter was applied to these images to reduce high-frequency, localized variations resulting from date differences in the

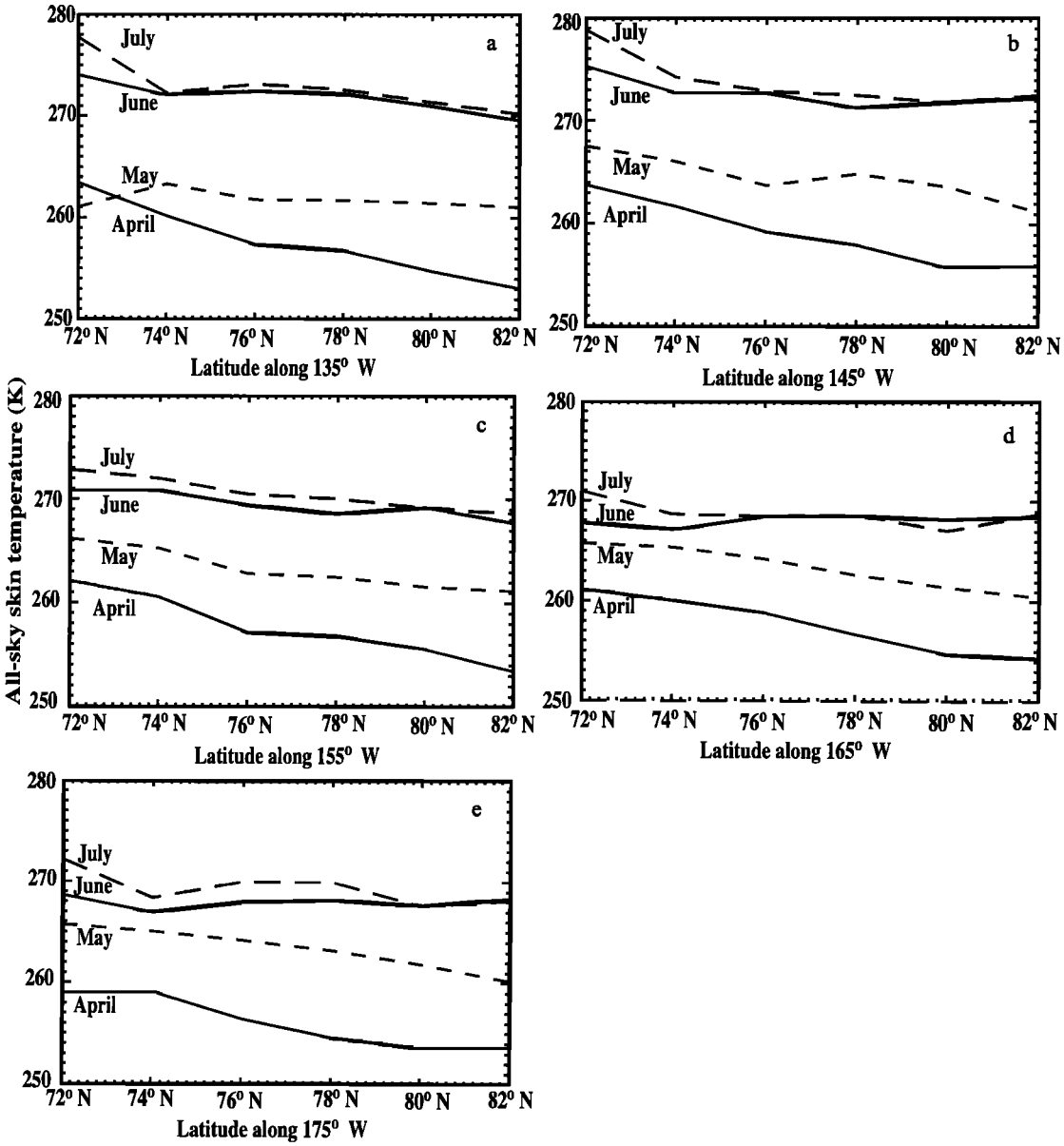

Figure 8. Monthly mean AVHRR-derived all-sky skin temperature for 105 x 105 km^2 areas centered on 2° latitude increments from 72°N to 82°N, along (a) 135°W longitude, (b) 145°W, (c) 155°W, (d) 165°W, and (e) 175°W.

composites. Open water is beginning to form in April along the eastern Beaufort coast, with a decrease in albedo elsewhere in the eastern and southern Beaufort Sea, probably due to the presence of open water and thin ice. Even at 5-km resolution some indications of large leads can be seen. By July (Figure 12) the unusually large expanse of open water is clearly shown. The July composite also suggests a large, relatively distinct region of reduced albedo within the consolidated ice pack, between Barrow and the SHEBA site. By September this region had become ice free. Since the compositing process uses data for the last clear-sky day encountered, the timing during the month when the last clear sky day occurred affects the composites. However, in these cases, the date used occurred fairly consistently within the last two weeks of each month. For Figure 12 the boundary between the lower-albedo region south of the SHEBA site and the higher albedo area to the north does not correspond to different days, and the dates used vary by only 3 days over much of the area shown. Within the region of reduced albedo, ice concentration was relatively high in July, based on the NIC ice charts, SSM/I data, and observations made during the NCAR C-130 flights to and from the SHEBA site. The visual observations during the C-130 flights suggest that the pack consisted mainly of first-year ice in this area, with extensive melt pond coverage. However, additional analysis of the SHEBA and FIRE observations are needed to determine the nature of this albedo variability.

Monthly means of the all-sky broadband albedo show the seasonal progression as well, with less noise but some loss of resolution due to the time averaging as well as to the local spatial interpolation used to create the all-sky products. The all-sky grids are better suited to modeling applications though, and maps of data for individual days (not shown) can be examined to provide increased detail. As with the summaries for the SHEBA region, the broader-scale maps of albedo agree well with other estimates derived from satellite imagery [e.g., *Scharfen et al.*,

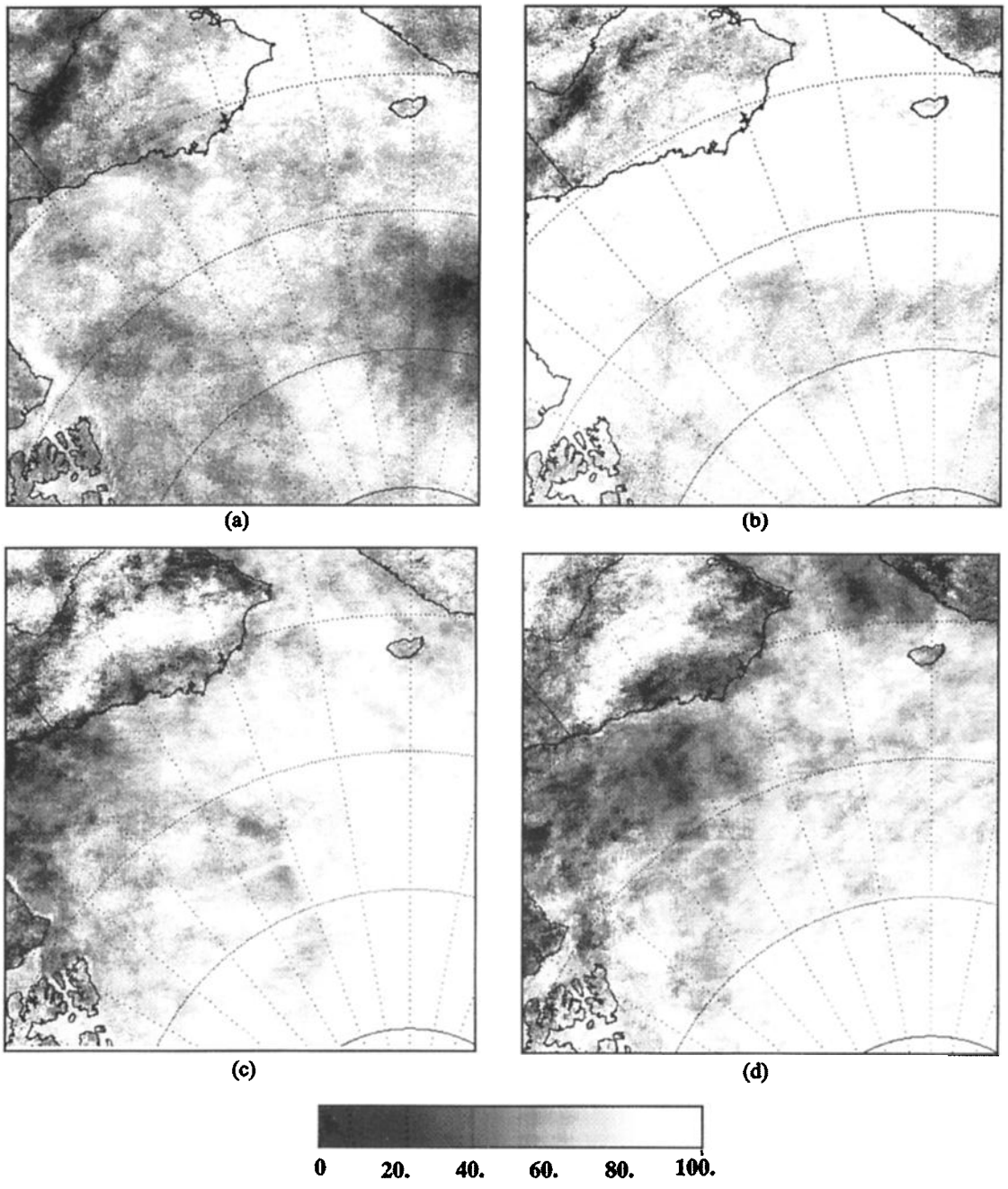

Figure 9. Monthly mean AVHRR-derived cloud amount (percent) for (a) April, (b) May, (c) June, and (d) July 1998.

1987; Lindsay and Rothrock, 1994]. The APP albedos are generally higher than those calculated by *Schweiger et al.* [1993] from International Satellite Cloud Climatology Project (ISCCP) reflectance data [*Rossow and Schiffer, 1991*] for earlier years, but are quite similar to the manually-derived albedos generated by *Robinson et al.* [*1992*] and analyzed by *Schweiger et al.* [1993]. Excluding the above-normal expanse of open water in 1998, the AVHRR-derived albedos within the ice pack in mid summer 1998 do not suggest an overall decrease compared to years summarized in these previous works. Instead, as noted above, the variations appear to be more localized. However, more work is needed to investigate whether the timing or rate of decrease in albedo differed significantly from other years.

Monthly means of all-sky skin temperature (not shown) describe a transition from a south-to-north increase in skin temperature in April and May to a meridional pattern in June and July. This concurs with the SLP patterns and variations in cloud fraction noted above. In these latter months, higher temperatures occur in the eastern portion of the study area, with increasing temperatures seen in the southeastern Beaufort Sea in conjunction with the reduction in ice cover. A similar but less distinct progression is seen in the NCEP surface air temperature fields. These patterns are also consistent with the record high temperatures observed in the Canadian archipelago region in 1997-1998 [*Maslanik et al., 1999a*].

The combination of decreased cloud cover in July as seen

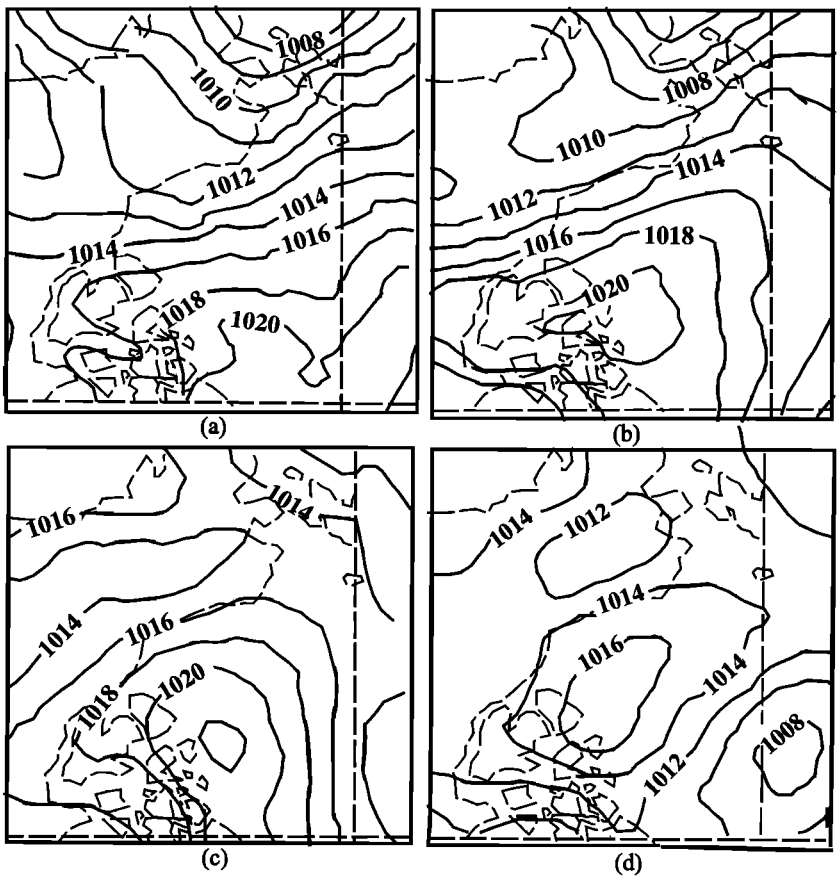

Figure 10. Monthly mean sea level pressures (hectaPascals) from National Centers for Environmental Prediction gridded fields for (a) April, (b) May, (c) June, and (d) July 1998.

earlier in Figure 9, above-normal air temperatures, and the increase in open water area yields the potential for considerable absorption of heat in the ice-free area, which would have accelerated ice melt and perhaps affected subsequent ice formation in autumn. This region of heating is illustrated well in a composite of clear-sky skin temperatures for July (Plate 1). The AVHRR data suggest a plume of Mackenzie River water with temperatures of 282 K - 284 K in the center of the plume, extending westward from the Mackenzie Delta with cooler water adjacent to the coast, as noted by *Macdonald et al. [1999]*. These AVHRR-derived temperatures are similar to typical measured Mackenzie River outflow temperatures *[Macdonald et al, 1989]*. To gain more insight into this warming of the ocean surface, open water skin temperatures were estimated from the AVHRR temperatures for July. This was done by assigning an assumed melting point skin temperature of 273.12 K for ice and then weighting by the SSM/I ice concentrations. Figure 13 shows the estimated open water skin temperature averaged over SSM/I-derived ice concentration categories. The plot suggests that relatively warm water can occur within the marginal ice zone, consistent with the heating in leads observed at the SHEBA camp *[Pegau and Paulson, 1999]* and in our preliminary analyses of NCAR C-130 aircraft data. The latter indicate open water lead temperatures of approximately 275 K in the surface layer of many leads in the vicinity of the SHEBA camp in July. The results in Figure 13 are, however, also affected by the influx of relatively warm Mackenzie River waters either by the effects of the warmer river water itself or by the production of a strongly stable surface layer that limits vertical mixing and thus keeps absorbed solar energy near the surface *[Macdonald et al, 1999]*. Since much of the area covered by the lower ice concentrations occurred in the Beaufort Sea, such mixing makes it difficult to determine from these data whether temperatures considerably above freezing are typical of marginal ice zones elsewhere in summer. The effects of the Mackenzie River waters, however, cannot account for the above-freezing temperatures within the high-concentration portions of the ice pack. This suggests that solar heating of the surface layer in leads is the most likely source for the above-freezing temperatures. Use of the SSM/I-derived ice concentrations also introduces some error since concentrations tend to be underestimated during midsummer due to surface melt effects *[e.g., Cavalieri, 1992]*. However, adjusting the concentrations upward would result in even greater estimated open water temperatures.

5. Conclusions

New AVHRR-derived products were used to investigate the spatial and temporal variability of atmospheric and surface parameters in the FIRE-ACE/SHEBA study area, and to assess how well the local conditions reflect conditions elsewhere in the western Arctic. Comparisons of AVHRR products with observations at the SHEBA field camp show generally good agreement, although additional work is needed to further improve cloud detection and estimates of cloud properties. In particular, it is necessary to determine the underlying reasons for differences between the cloud retrievals from the various observing methods. This understanding should in turn help to reduce the

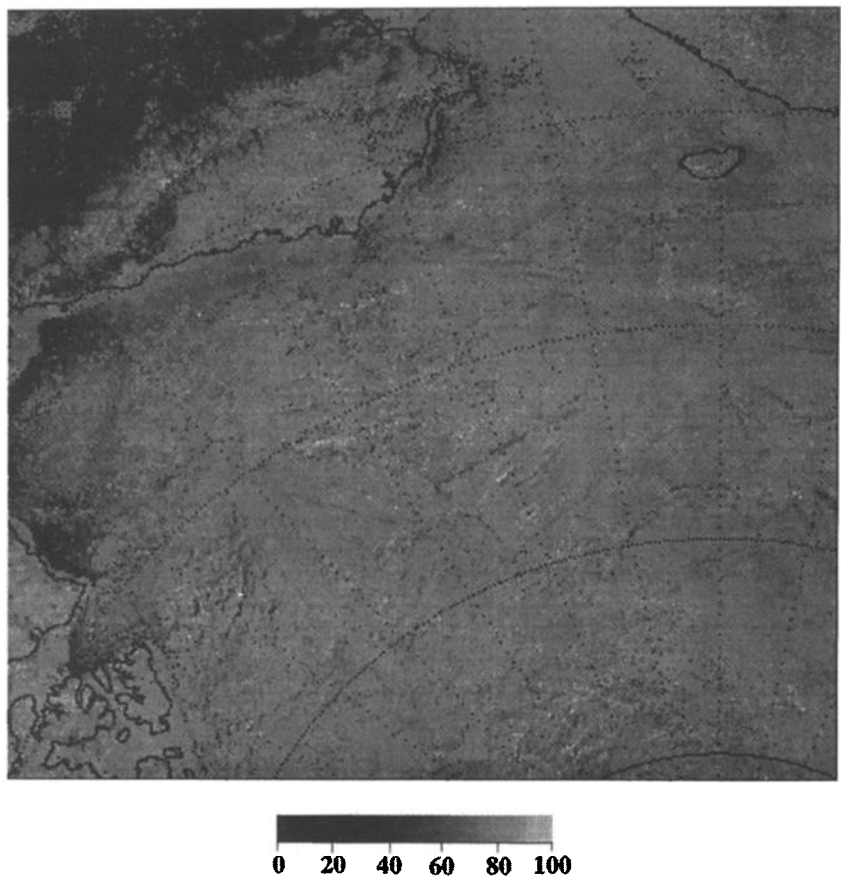

Figure 11. Composite of AVHRR-derived broadband clear-sky albedo for April.

discrepancies in radiative fluxes seen during part of the study period. In late summer, the discrepancies between S_{net} estimated from the AVHRR data and S_{net} observed at the surface are relatively large and would signficantly affect simulations of ice conditions. Mean cloud fraction is consistent with synoptic-scale atmospheric circulation, with a well-defined region of reduced cloud cover that develops by midsummer over the eastern and central Beaufort Sea. Statistics examining spatial and temporal correlations illustrate the degree to which the different parameters vary with changing scale. During the spring-summer period studied, clouds and radiation are most variable over short (5 to 25 km) distances and time periods, while surface temperature is more variable over larger scales. Comparisons over different space scales suggest that the field observations obtained at the SHEBA site are quire representative of the larger aggregate-scale area, although there is some indication that cloud cover may have been greater over the SHEBA site than elsewhere in the nearby, surrounding region.

The products considered here provide a suite of variables that can be studied jointly and at relatively fine spatial and temporal resolution. As a result, it is possible to observe the progression of change in surface conditions in conjunction with atmospheric forcings. Variations in albedo, temperature, cloud cover, and radiation are primarily zonal during April-May, becoming more meridional as summer progresses, consistent with the above-normal high-pressure cell that persisted over the eastern Beaufort Sea and Canadian archipelago. A large gradient in albedo developed by late summer, differentiating the seasonal and perennial ice zones. The large decreases in albedo seen in the Beaufort Sea were due to reductions in ice extent. Spatial variations in albedo in the Chukchi Sea south of the SHEBA site are less clearly linked to ice concentration and may represent differences in the evolution of albedo over first-year ice versus old ice.

The time series of skin temperatures reveals considerable warming of the open ocean area in the eastern Beaufort Sea. Stratifying the AVHRR-derived skin temperatures as a function of SSM/I-derived ice concentration suggests further that heating of open water within the ice pack contributes to surface temperatures that can be several degrees above the freezing point even when a substantial amount of ice is present. This contrasts with the assumption typically used in climate models, where open water is prescribed to remain at the freezing point until all ice is melted within a grid cell. However, because some of the observed warming reflects the localized effects of Mackenzie River runoff, more work is needed to investigate the variations of skin temperature within and near the ice pack in other areas. Since the Mackenzie River outflow was well above normal in recent years [*Macdonald et al., 1999*], this localized warming presumably provided an additional source of heat that could help account for reduced ice cover in the Beaufort Sea.

The reduction in cloud amount observed over the eastern Beaufort Sea, a tendency seen in cloud climatologies for this region, provides further potential for enhanced melt followed by further warming of the open ocean through absorption of solar radiation. The combination of reduced ice cover and increase in ocean temperatures in the eastern Beaufort Sea in spring-summer 1998 thus may represent a regional example of the effects of the ice-albedo feedback, which may have contributed to the record reductions in ice extent in this area. Prevailing wind patterns also

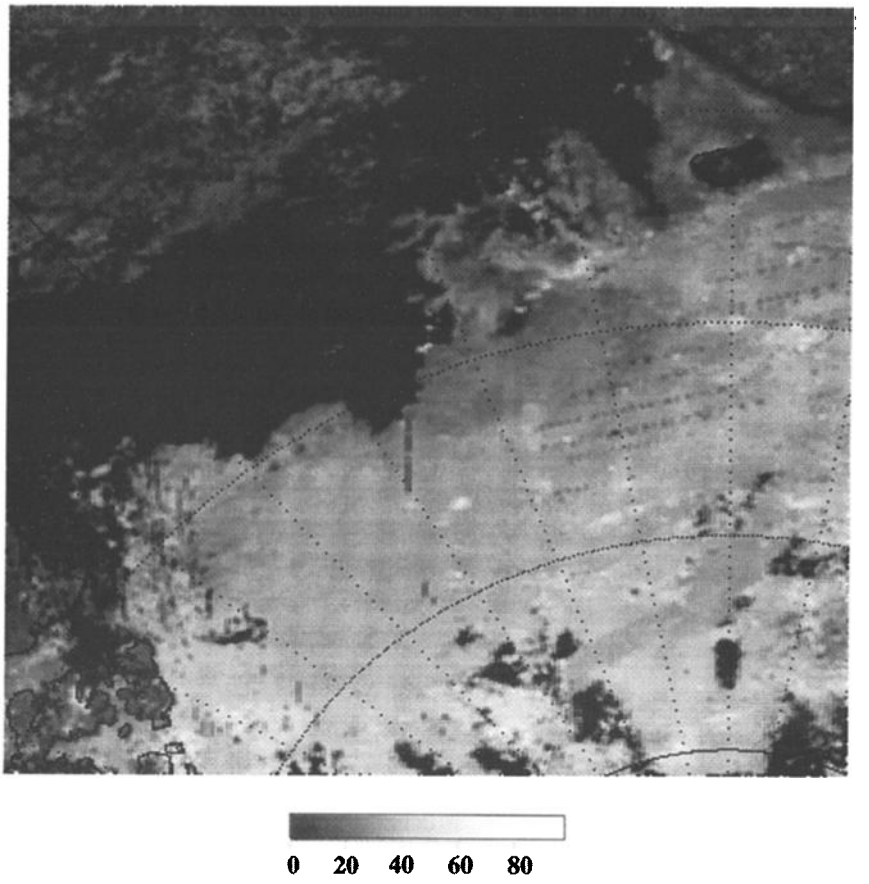

Figure 12. Composite of AVHRR-derived broadband clear-sky albedo for July. Black areas over the ice pack are areas that were continually cloud covered during the month.

favored production of additional open water area through dynamics and advection. This would have further reduced the albedo, leading to increasing melt and a thinner, weaker ice pack that may have been more susceptible to additional disruption and advection by winds and ocean currents. Such an ice dynamic-thermodynamic feedback appears to have contributed to similar, large reductions in regional ice cover in the Siberian Sea in 1990 [*Maslanik et al., 2000*]. The detailed and extensive field data sets acquired during SHEBA and FIRE-ACE, along with satellite-derived products, buoy data, and improved forecast model output, should provide the means to further diagnose conditions during 1998 in comparison to previous years and will contribute to testing and improving the ability of models to simulate such events.

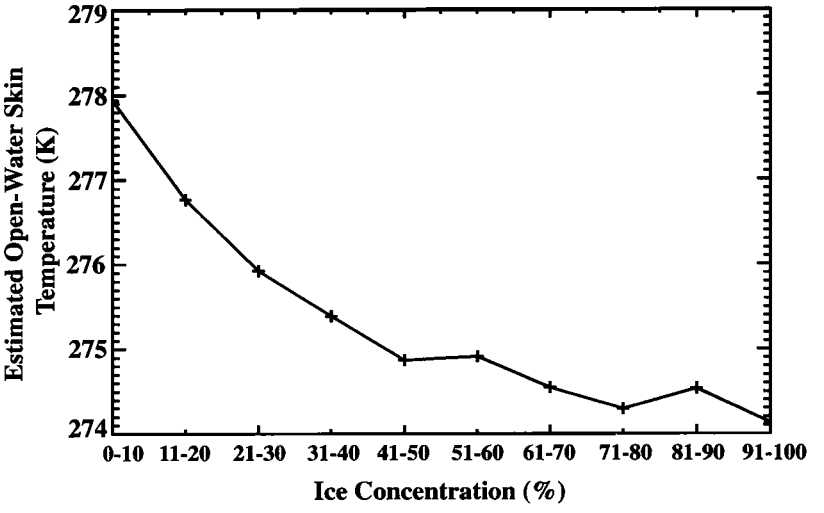

Figure 13. Estimated mean open water skin temperatures for July 1998 derived from AVHRR skin temperatures stratified by SSM/I-derived ice concentration categories.

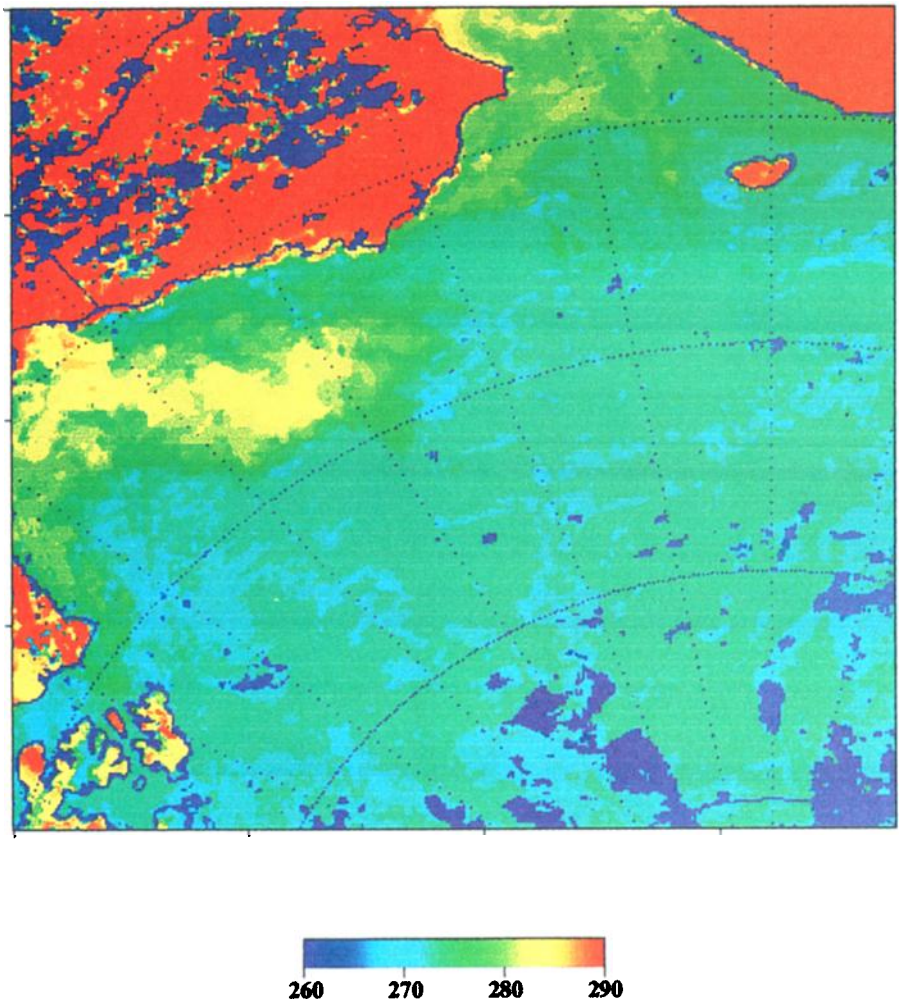

Plate 1. Composite of AVHRR-derived clear-sky skin temperature for July.

Appendix A: Description of Satellite Algorithms

In this section the algorithms used to estimate surface and cloud properties from satellite data are briefly described. Validation of these parameters is discussed in the references provided. See *Key* [2000] for additional details and references.

Calibration of the shortwave visible and near-infrared channels of the AVHRR (channels 1 and 2 at 0.6 and 0.9 μm, respectively) is done according to *Rao* [1993], which corrects for sensor drift over time. Channels 1 and 2 are further adjusted for Earth-Sun distance. The standard NOAA/NESDIS method [*NOAA, 1991*] is used for the calibration of the thermal channels (3, 4, and 5 at 3.7, 11, and 12 μm), with the addition of a correction for non linearity.

At 3.7 μm, AVHRR channel 3 contains both reflected solar and emitted thermal components. The reflected portion is approximated by removing from the total radiance an estimate of the emitted portion based on the temperature of channel 4:

$$\rho_3 = \frac{L_3 - B_3(T_4)}{L_0\mu - B_3(T_4)}, \qquad \text{(A1)}$$

where ρ_3 is the channel 3 reflectance, L_3 is the channel 3 radiance, $B_3(T_4)$ is the Planck function for channel 3 based on the channel 4 temperature T_4, L_0 is the solar constant for the band adjusted for Earth-Sun distance, and μ is the cosine of the solar zenith angle.

A1. Surface Temperature

For the retrieval of clear-sky surface temperature a simple regression model is used to correct for atmospheric attenuation. For high-latitude ocean and snow-covered land we use the equation

$$T_s = a + bT_4 + c(T_4 - T_5) + d[(T_4 - T_5)(\sec\theta - 1), \qquad \text{(A2)}$$

where T_s is the surface temperature, T_4 and T_5 are the satellite-measured brightness temperatures in channels 4 and 5, θ is the sensor scan angle, and a, b, c, and d are regression coefficients. To determine the empirical relationship radiosonde data from drifting ice and land stations in the Arctic and Antarctic were used with a radiative transfer model to simulate the sensor brightness temperatures. The surface temperature retrieval methods for both sea ice/snow and snow-free land are described in detail by *Key, et al.* [1997].

The cloudy sky surface temperature calculation is based on empirical relationships among the clear-sky temperature, wind speed, and solar zenith angle (daytime), determined using surface observations from the SHEBA experiment. For the polar night

and before the melt season (November through April) there are two equations: (1) solar zenith angle 80° or more ($T_{cld} = a_1 + b_1*T_{clr} + c_1*u_{cld}$) and (2) solar zenith angle less than 80° ($T_{cld} = a_2 + b_2*T_{clr} + c_2*\cos(Z) + d_2*u_{cld}$). During the warm season, defined as May-September with the surface temperature greater than 255 K, the following apply: (1) solar zenith angle less than 90° ($T_{cld} = a_3 + b_3*T_{clr} + c_3*\cos(Z)$), and (2) nighttime only ($T_{cld} = a_4 + b_4*T_{clr} + c_4*u_{cld}$), where T_{cld} is the cloudy sky surface temperature (K), T_{clr} is the clear sky surface temperature (K), u_{cld} is the cloudy sky wind speed (m s^{-1}) from the SHEBA ship observations, and Z is the solar zenith angle. In the application of the above equations the clear-sky surface temperatures (T_{clr} here and T_s in equation (A1)) are interpolated to cloudy pixels with a kriging function, and the cloudy sky temperatures are then estimated. The cloudy sky surface temperature retrieval procedure is detailed by X. Wang and J. Key (Estimating the cloudy sky surface temperature of sea ice from space, submitted to *Journal of Geophysical Research, 2000*). Comparisons with SHEBA surface observations yield a bias (mean error) of –1.6 K and a root-mean-square error (rmse) of 6 K for the all-sky surface temperature. A negative bias indicates that the satellite retrieval is less than the surface observation. Comparisons to three International Arctic Buoy Program (IABP) buoys located from approximately 20 km to 450 km from the *Des Groseilliers* in April-July 1998 show that the AVHRR temperatures track the temporal variability of the buoy temperatures quite well, with mean monthly differences typically less than 2 K.

A2. Surface Albedo

The retrieval of surface albedo involves four steps. First the clear-sky albedo is estimated by converting channels 1 and 2 narrowband reflectances to a broadband reflectance, correcting the top-of-atmosphere (TOA) broadband reflectance for anisotropy, and converting the TOA broadband albedo to a surface broadband albedo. The cloudy-sky albedo is then estimated by adjusting the surface clear-sky broadband albedo for the effects of cloud cover in cloudy pixels. The albedo presented here is a directional-hemispherical apparent albedo, where "apparent" albedo is what would be calculated using uplooking and downlooking radiometers in the field. The calculated surface albedo therefore varies with atmospheric conditions and the solar zenith angle.

The narrowband-to-broadband conversion takes the form

$$\rho_{toa} = a + b\rho_{1,toa} + c\rho_{2,toa} \tag{A3}$$

where $\rho_{1,toa}$ is the channel 1 reflectance, $\rho_{1,toa}$ is the channel 2 reflectance, ρ_{toa} is the broadband TOA reflectance, and a, b, and c are regression coefficients. To develop the regression relationship the radiative transfer model Streamer [*Key and Schweiger, 1998*] was used to simulate the TOA reflectances over a broad range of viewing and illumination angles, atmospheric conditions, and surface types and albedos.

A correction for the dependence of the sun-satellite-surface geometry on reflectance was done with data presented by *Suttles et al.* [1988], who used ERBE and GOES data to determine TOA anisotropic reflectance factors (ARF) for the broad shortwave band over various surfaces. The correction is

$$\alpha_{toa} = \frac{\rho_{toa}}{f}, \tag{A4}$$

where ρ_{toa} is the reflectance observed at the sensor (simulated by *Streamer* in step 1), f is the anisotropic reflectance factor, and α_{toa} is the TOA albedo, which is only a function of solar zenith angle.

Next, the broadband, clear sky, apparent surface albedo is estimated with a regression relationship of the form

$$\alpha_{toa} = a + b\alpha_s, \tag{A5}$$

where α_s is the surface reflectance, and a and b are a function of water vapor, aerosol amount, and solar zenith angle. The coefficients were determined with Streamer.

The surface albedo under clear and cloudy conditions can be very different. This is particularly true for snow, where the albedo under a thick cloud may be 15-20% higher than the clear-sky value. The albedo of cloudy pixels is determined using the clear sky albedo, interpolated to fill in the entire image, and adjusted by the cloud optical depth and the solar zenith angle. The cloud optical depth calculation is described by *Key* [2000]. The conversion from clear to cloudy albedo is also based on model calculations, yielding the empirical relationship

$$\alpha_{s,cld} = a + b\alpha_{s,clr} + c\ln(\tau + 1) + d\cos Z, \tag{A6}$$

where τ is the cloud visible optical depth (unitless), $\alpha_{s,clr}$ is the clear sky apparent albedo, Z is the solar zenith angle, and a, b, and c are regression coefficients. This relationship works best when the snow surface is bright ($\alpha > 0.5$) and clouds have small to moderately large optical depths ($1 < \tau < 50$). The surface albedo retrieval procedure is detailed by J. Key et al. (Estimating the clear-sky and cloudy-sky surface albedo of snow and sea ice from space, submitted to *Journal of Geophysical Research*). Comparisons with SHEBA surface observations yield a bias of –0.028 and a rmse of 0.08 for the all-sky surface albedo.

A3. Cloud Detection

The cloud-masking procedure consists of thresholding operations that are based on modeled sensor radiances. The AVHRR radiances are simulated for a wide variety of surface and atmospheric conditions, and values that approximately divide clear from cloudy scenes are determined. In the presence of sunlight (daytime) the spectral cloud tests work well in that false detections (labeling clear pixels as cloudy) are infrequent. So the daytime algorithm uses only spectral tests and is conceptually simple: initialize the cloud mask to clear then apply the cloud tests to label cloudy pixels.

In the absence of sunlight the procedure is different because there is less spectral information available and because AVHRR channel 3 tends to be noisy at low temperatures, common during the polar night. Under most conditions, optically thick clouds simply cannot be distinguished from clear sky with the three thermal channels alone. The nighttime algorithm first applies the spectral cloud tests, resulting in some false detections for noisy pixels and for optically thick clouds. The spectral test thresholds are set to be clear-conservative to increase the likelihood that those pixels labeled as clear are in fact clear. Next a clear-sky channel 4 temperature image is constructed by passing a mean filter over the clear pixels, eliminating much of the noise and false detections. The image is then rethresholded on the basis of the clear-sky map such that temperature departures more than some number of degrees from the clear-sky mean signifies that a pixel is cloudy. In this final thresholding it is possible for the cloud to be either warmer or colder than the surface, especially during the winter.

Many of the cloud test concepts can be found in the Air Force SERCAA procedures [*Gustafson et al., 1994*]; some appear in the NOAA CLAVR algorithm [*Stowe et al., 1991*]; most were developed and/or used elsewhere. In the discussion below, "warm" cloud refers to clouds that have higher temperatures than the surface, while "cold" clouds have temperatures lower than the surface. The cloud tests are as follows:

A3.1. Cirrus test, 11-12 μm (day and night). A pixel is cloudy if BTD45 > CCT_TABLE, where BTD45 is channel 4 minus channel 5 brightness temperature difference and CCT_TABLE is a table of thresholds from *Saunders and Kriebel* [1988], extended to include lower temperatures (range 230-310 K). The thresholds are the expected maximum BTD45 for clear sky.

A3.2. Warm clouds, 11-12 μm (day and night). For warm clouds, BTD45 may be negative so an additional test is required [cf. *Yamanouchi et al., 1987*]. A pixel is considered to be cloudy if BTD45 < WARM45. This test is most applicable at night in the presence of a temperature inversion.

A3.3. Water cloud test, 3.7 μm (day only). A pixel is considered cloudy if REF3 > REF3_THRESH and REF1 > REF1_THRESH, where REF1 and REF3 are the channels 1 and 3 reflectances and REF1_THRESH and REF3_THRESH are threshold values.

A3.4. Low stratus, thin cirrus tests, 3.7-11 μm (night only). A pixel is cloudy if BTD34 <= LSTTCI_34LO or BTD34 >= LSTTCI_34HI, where BTD34 is the brightness temperature difference between channels 3 and 4.

Additional details are provided by *Key* [2000]. Comparisons with SHEBA surface observations of cloud amount (three-hourly synoptic observations) yield a bias of 0.1 and a rmse of 0.3.

A4. Cloud Particle Phase

All clouds are considered here to be composed of either liquid droplets ("water cloud") or ice crystals ("ice cloud"). No attempt is made to identify mixed-phase or multilayer clouds. The determination of cloud particle thermodynamic phase is based on both physical and spectral properties. Physically, liquid cloud droplets can exist at temperatures as low as -40° C, although clouds are likely to be composed of both liquid droplets and ice crystals at temperatures below -10° C. The spectral difference between water and ice clouds occurs because of differences in absorption and scattering.

For optically thick clouds, where the transmittance is near zero and the surface contribution to upwelling radiance is small, absorption and scattering define the spectral characteristics of a cloud. We expect the brightness temperature difference between channels 3 and 4, BTD34, to be negative for water clouds with small effective radii. For thick ice clouds with particle effective radii of 30 μm or larger, the single-scattering albedo indicates that BTD34 would be near zero. For optically thin clouds the transmissivity is not negligible and the surface temperature influences the brightness temperature measured at the satellite. BTD34 for cold water clouds (surface is warmer than the cloud) is positive when the optical depth is small. BTD34 for ice clouds takes on larger positive values in these cases. The opposite occurs for warm ice clouds, where BTD34 is negative. The brightness temperature difference between 11 and 12 μm, BTD45, is much smaller than BTD34 for both water and ice clouds, and there is considerable overlap in BTD45 for the two phases. The absolute value of BTD45 increases as cloud optical depth decreases. Therefore large BTD45 differences (positive or negative) indicate thin clouds.

In the presence of solar radiation the single-scattering albedo at 3.7 μm is the primary spectral feature used in distinguishing ice and water cloud. Ice particles do not scatter so efficiently as water droplets at this wavelength, because of both their indices of refraction (the real part) and the fact that ice clouds are typically composed of larger particles, which scatter less efficiently, than water clouds. However, the actual 3.7 μm reflectance depends not only on particle phase but also on viewing and illumination geometry and surface reflectance.

The phase algorithm starts by exploiting the physical property that only ice crystals will exist below some threshold temperature, and only liquid droplets will exist above some other threshold temperature. The next step employs the spectral properties described above and is different for day and night conditions. It is applied to the cloudy pixels that were not labeled in the first step. At night the tests are based on brightness temperature differences and are intended to identify optically thick ice cloud, thick water cloud, and most thin water cloud. During the day the tests are based on the 3.7 μm reflectance and the scattering angle, where an empirical function based on modeled reflectances is used to define a threshold. The last step is to label any pixels that where not handled by the previous two steps. A simple temperature threshold is employed: if the 11 um brightness temperature is less than 258.16 K (-15° C), then the cloud phase is ice, otherwise it is liquid. Because of the low precision and high uncertainty in T_3 (and therefore T_3-T_4) when temperatures are very low, all pixels with T_4 less than 230 K are labeled as ice. Comparisons with SHEBA lidar observations for single-layer, single-phase clouds shows 95% accuracy. *Key and Intrieri* [2000] describe the particle phase procedure in detail.

A5. Cloud Top Temperature and Pressure

The cloud top temperature is determined from the channel 4 brightness temperature, the clear sky brightness temperature, and the visible cloud optical depth. The infrared optical depth is determined from the visible optical depth using parameterizations of cloud optical properties described by*Key* [2000]. If the slant path thermal optical depth is less than some threshold, the brightness temperature is assumed to be a function of both the cloud temperature and the upwelling radiation from the surface and atmosphere below the cloud. The threshold is taken from the ISCCP processing scheme, chosen such that clouds with optical depths greater than the threshold have transmittances of less than 1% (equivalent to an optical depth of 4.6) and are considered opaque. For opaque clouds the cloud top temperature is simply the channel 4 temperature. If the cloud is not opaque, then the cloud temperature is determined by first computing the cloud transmittance t from the infrared optical depth, then calculating the cloud radiance that would be required to produce the observed radiance of the cloudy pixel, given the cloud optical thickness and the observed clear-sky radiance (as an approximation of the surface radiance under the cloud):

$$L_c = \frac{L_4 - tL_{clr}}{1 - t}, \qquad \text{(A7)}$$

where L_c is the cloud radiance, L_4 is the channel 4 radiance, and L_{clr} is the clear sky radiance. If the estimated surface temperature is too low and the cloud is thin, then the cloud top temperature will be too high and vice versa. If the adjusted cloud top temperature is either lower than the tropopause temperature or higher than the maximum temperature from 950 hPa to the

tropopause, then it is reset to either the minimum or the maximum temperature, as appropriate.

The location of the cloud top, i.e., the cloud top pressure, is determined by searching the radiosonde temperature profile from the top down. With this scheme, if a cloud has a temperature that could be either within or above an inversion, it will be placed above. This choice is arbitrary, although it was shown to give better results when compared to surface-based lidar retrievals. Cloud top temperature and pressure are currently being validated with SHEBA lidar and radar measurements.

A6. Radiative Fluxes

Upwelling and downwelling shortwave and longwave fluxes at the surface are computed with a neural network trained to simulate a radiative transfer model. The neural network, called FluxNet [*Key and Schweiger, 1998*], was trained to simulate Streamer. Root-mean-square differences between the neural network and the radiative transfer model for downwelling shortwave and longwave fluxes at the surface are of the order of 2-3% with biases near zero. The advantage of *FluxNet* is that it is 100 to 10,000 times faster than *Streamer*, making it ideal for processing satellite image data. Inputs to *FluxNet* are surface temperature, surface albedo, surface type, cloud particle phase, effective radius, optical depth, and pressure, total precipitable water, aerosol visible optical depth, and total column ozone. The surface and cloud properties are retrieved from the AVHRR. Precipitable water is derived from the SHEBA radiosonde profiles, aerosol optical depth is set to 0.06, and a value of 325 DU (Dobson units) is used for total column ozone.

Comparisons of computed downwelling shortwave radiation with SHEBA surface observations yield a bias of –9 W m^{-2} and a rmse of 100 W m^{-2}. For the downwelling longwave flux the bias and rmse are 11 and 42 W m^{-2}, respectively. The rmse values are large because the radiative fluxes are based on retrieved quantities, each with their own rmse. This topic is addressed in detail by *Key et al.* [1997].

Acknowledgments. Support for this work was provided by the National Science Foundation and NASA. Thanks are due to T. Uttal, J. Intrieri, M. Shupe (NOAA), and the SHEBA Project Office for providing SHEBA data for comparison. IABP buoy data were provided by M. Ortmeyer and I. Rigor of the University of Washington. Sea ice concentration data were obtained from the National Snow and Ice Data Center. AVHRR data were obtained with the assistance of the Jet Propulsion Laboratory, NOAA Satellite Active Archive, and the University of Colorado DOMSAT facility. The Polar Pathfinder products are available from NSIDC (NSIDC (http://www-nsidc.colorado.edu). We would also like to thank the many other individuals who assisted in the collection of SHEBA and FIRE-ACE data, including the crew of the *Des Groseilliers*.

References

Armstrong, R.L., and M.J. Brodzik, An Earth-gridded SSM/I data set for cryospheric studies and global change monitoring, *Adv. Space Res.*, 16(10), 155-163., 1995.

Cavalieri, D.J., The validation of geophysical products using multisensor data. in *Microwave Remote Sensing of Sea Ice*, *Geophys. Monogr. Ser.* vol. 68, edited by F. Carsey, pp. 233-242, AGU, Washington, D.C., 1992.

Gustafson, G.B., et al., Support of Environmental Requirements for Cloud Analysis and Archive (SERCAA), *Sci. Rep. 2, PL-TR-94-2114*, 100 pp., Phillips Laboratory, Hanscom Air Force Base, Mass., 1994

Key, J., *The Cloud and Surface Parameter Retrieval (CASPR) System for Polar AVHRR*, 59 pp., Coop. Inst. for Meteorol. Satell. Stud., Univ. of Wisc., Madison, 2000.

Key, J. and J. Intrieri, Cloud particle phase determination with the AVHRR, *J. Appl. Meteorol.*, in press, 2000.

Key, J., and A.J. Schweiger, 1998, Tools for atmospheric radiative transfer: Streamer and FluxNet, *Comput. and Geosci.*, *24*(5), 443-451, 1998.

Key, J., A.J. Schweiger, and R.S. Stone, Expected uncertainty in satellite-derived estimates of the high-latitude surface radiation budget, *J. Geophys. Res.*, *102*, 15,837-15,847, 1997a.

Key, J., J. Collins, C. Fowler, and R.S. Stone, High-latitude surface temperature estimates from thermal satellite data, *Remote Sens. Environ.*, *61*, 302-309, 1997b.

Lindsay, R.W. and D.A. Rothrock, Arctic sea ice albedo from AVHRR, *J. Clim.*, *7*(11), 1737-1749, 1994.

Macdonald, R.W., E.C. Carmack, F.A. McLaughlin, K Iseki, D.M. Macdonald, and M.C. O'Brian, Composition and modification of water masses in the Mackenzie Shelf Estuary, *J. Geophys Res.*, *94*, 18,057-18,070, 1989.

Macdonald, R W., E.C. Carmack, F.A. McLaughlin, K.K. Falkner, and J.H. Swift, Connections among ice, runoff and atmospheric forcing in the Beaufort Gyre, *Geophys. Res. Lett.*, *26*(15), 2223-2226, 1999.

Maslanik, J., C. Fowler, J. Key, T. Scambos, T. Hutchinson, and W. Emery, AVHRR-based Polar Pathfinder products for modeling applications, *Ann. of Glaciol.*, *25*, 388-392, 1998.

Maslanik, J.A. M.C. Serreze, and T. Agnew, On the record reduction in western Arctic sea-ice cover in 1998, *Geophys. Res. Lett. 26*(13), 1905-1908, 1999a.

Maslanik, J.A., A. Lynch, and C. Fowler, 1999b. Assessing 2-D and coupled-model simulations of sea ice anomalies using remotely-sensed polar pathfinder products, in *Fifth Conference on Polar Meteorology and Oceanography*, pp. 476-479, Am. Meteorol. Soc., Boston, Mass., 476-479, 1999b.

Maslanik, J.A., A.H. Lynch, M.C. Serreze, and W. Wu, A case study of regional climate anomalies in the Arctic: Performance requirements for a coupled model, *J. Clim.*, *13*, 383-401, 2000.

McPhee, M.G., T.P. Stanton, J.H. Morison, and D.G. Martinson, Freshening of the upper ocean in the central Arctic: Is perennial ice disappearing?, *Geophys. Res. Lett.*, *23*, 1677-1680, 1998.

Meier, W.N., J.A. Maslanik, J.R. Key, and C.W. W. Fowler, Multiparameter AVHRR-derived products for Arctic climate studies, *Earth Inter.*, *1*, 1997. (Available at http://EarthInteractions.org)

Moritz, R.E and D.K. Perovich, Eds., SHEBA, a research program on the Surface Heat Budget of the Arctic Ocean: Science plan, ARCSS/OAII Rep. *5*, 60 pp., Polar Sci. Cent., Univ. of Wash., Seattle, 1996.

National Oceanic and Atmospheric Administration (NOAA), *NOAA Polar Orbiter Data User's Guide*, U.S. Dep. of Comm., Nat.. Oceanic and Atmos. Admin., NESDIS, Washington, D.C., February, 1991.

Pegau, W.S. and C.A. Paulson, The role of summer leads in the heat and mass balance of the upper Arctic Ocean, in *Fifth Conference on Polar Meteorology and Oceanography*, pp 401-403, Am. Meteorol. Soc., Boston, Mass., 1999.

Rao, C.R.N., 1993, Degradation of the visible and near-infrared channels of the advanced very high resolution radiometer on the NOAA-9 spacecraft: assessment and recommendations for corrections *NOAA Tech. Rep NESDIS 70*, 25 pp., U.S. Dep. of Comm., 1993.

Robinson, D.A. M.C. Serreze, R.G. Barry, G. Scharfen, and G. Kukla, Large-scale patterns and variability of snow melt and parameterized surface albedo in the Arctic Basin, *J. Clim.*, *5*(10), 1109-1119, 1992.

Rogers, J.C., Meteorological factors affecting interannual variability of summertime ice extent in the Beaufort Sea, *Mon. Weather Rev.*, *106*(6), 890-897, 1978.

Rossow, W.B. and R.A. Schiffer, ISCCP cloud data products, *Bull. Am. Meteorol. Soc.*, 72, 2-20, 1991.

Saunders, R.W., and K.T. Kriebel, An improved method for detecting clear sky and cloudy radiances from AVHRR data, *Int. J. Remote Sens.*, *9*(1), 123-150, 1988.

Scharfen, G., R.G. Barry, D A. Robinson, G. Kukla, and M.C. Serreze, Large-scale patterns of snow melt on Arctic sea ice mapped from meteorological satellite imagery. *Ann. Glaciol.*, *9*, 1-6, 1987.

Schweiger, A.J., and J.R. Key, Arctic cloudiness: Comparison of ISCCP-C2 and Nimbus-7 satellite-derived cloud products with a surface-based cloud climatology, *J. Clim.*,*5*(12), 1514-1527, 1992.

Schweiger, A.J., M.C. Serreze, and J.R. Key, Arctic sea ice albedo: A comparison of two satellite-derived data sets, *Geophys. Res. Lett.*, *20*(1), 41-44, 1993.

Schweiger, A., et al., P-Cube: A multisensor data set for polar climate research, in *5th. Conference on Polar Meteorology and Oceanography*, pp. 136-141, Am. Meteorol. Soc., Boston, Mass., 1999.

Serreze, M.C. and M.C. Rehder, 1990. June cloud cover over the Arctic Ocean, *Geophys. Res. Lett.*, *17*(12) 1397-2400, 1990.

Serreze, M.C., J.A. Maslanik, and J.R. Key, Atmospheric and sea ice characteristics of the Arctic Ocean and the SHEBA field region in the Beaufort Sea. Nat. Snow Ice Data Cent. Spec. Rep. *4*, 217 pp., Univ. of Colo., Boulder, CO 80309, 1997.

Stowe, L.L., E.P. McClain, R. Carey, P. Pellegrino, and G.G. Gutman, Global distribution of cloud cover derived from NOAA/AVHRR operational satellite data, *Adv. Space Res.*, *11*(3), 51-54, 1991.

Suttles, J.T., R.N. Green, P. Minnis, G.L. Smith, W.F. Staylor, B.A. Wielicki, I.J. Walker, D.F. Young, V.R. Taylor, and L.L. Stowe, Angular radiation models for Earth-Atmosphere system, Shortwave radiation, *NASA Ref. Pub. 1184*, vol. 1, 144 pp., 1988.

Warren, S.G., C.J. Hahn, J. London, R.M. Chervin, and R. Jenne, Global distribution of total cloud cover and cloud type amounts over land, *NCAR Tech. Note TN-273+STR*, 29 pp., Natl. Cent. for Atmos. Res., Boulder, Colo., 1986.

Warren, S.G., C.J. Hahn, J. London, R.M. Chervin, and R. Jenne, 1988 Global distribution of total cloud cover and cloud type amounts over the ocean, *NCAR Tech. Note TN-317+STR*, 41 pp., Natl. Cent. for Atmos. Res., Boulder, Colo., 1988.

Yamanouchi, T., K. Suziki, and S. Kawaguchi, Detection of clouds in Antarctica from infrared multispectral data of AVHRR, *J. Meteorol. Soc. Jpn.*, *65*(6): 949-961, 1987.

C. W. Fowler, J. Maslanik, and T. Nguyen, University of Colorado, CCAR, CB431, Boulder, CO 80309. (cfowler@frodo.colorado.edu, james.maslanik@colorado.edu)

J. Key and X. Wang, Cooperative Institute for Meteorological Satellite Studies, University of Wisconsin, 1225 W. Dayton St., Madison, WI 53706. (jkey@ssec.wisc.edu)

(Received December 21, 1999; revised April 24, 2000; accepted May 4, 2000.)